Macromolecules

Article

pubs.acs.org/Macromolecules

Lyotropic Liquid Crystal of Polyacrylonitrile-Grafted Graphene Oxide and Its Assembled Continuous Strong Nacre-Mimetic Fibers

Zheng Liu, Zhen Xu, Xiaozhen Hu, and Chao Gao*

MOE Key Laboratory of Macromolecular Synthesis and Functionalization; Department of Polymer Science and Engineering, Zhejiang University, Hangzhou 310027, China

Supporting Information

ABSTRACT: Liquid crystals (LCs) of pristine graphene oxide (GO), a kind of novel two-dimensional (2D) macromolecule, have been discovered recently, opening an avenue to high performance neat graphene fibers. Here, we report for the first time LC of polymer-grafted GO and its macroscopic assembled nacre-mimetic composite. Polyacrylonitrile (PAN) chains were covalently and uniformly grafted onto GO surfaces via a simple free radical polymerization process. The PAN-grafted GO (GO-*g*-PAN) sheets were well dispersed in polar organic solvents such as dimethylformamide (DMF) and dimethyl sulfoxide (DMSO), forming nematic and lamellar LCs upon increasing concentration. A strong signal was found in the circular dichroism spectra of the LCs, indicating the formation of helical lamellar structures for the GO-*g*-PAN LCs. Macroscopic assembled fibers were continuously spun from the GO-*g*-PAN LCs via the industrially viable wet-spinning technology. The fibers held strict layered structures of GO and PAN, resembling the classic "brick-and-mortar" microstructure observed in nacre. The nacre-mimetic composite showed excellent mechanical property with tensile strength of 452 MPa, Young's modulus of 8.31 GPa, and breakage elongation of 5.44%. This offers a new approach for the fabrication of continuous, ultrastrong, and tough biomimic composites.

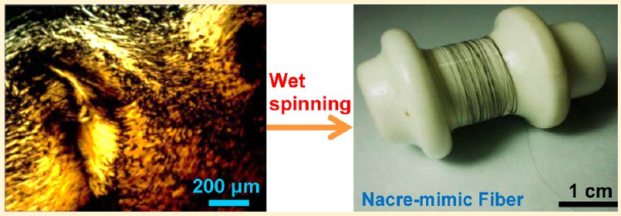

INTRODUCTION

Graphene can be regarded as a novel kind of two-dimensional (2D) carbon-based macromolecule.[1−6] Since its first finding in 2004, graphene has sparked enormous interest in science and technology communities due to its exceptional mechanical, electrical, thermal, and optical properties.[7−12] However, it is hard to directly process graphene due to its poor dispersibility in common solvents and nonfusible nature at an accessible temperature. Alternatively, graphene oxide (GO) appears as a very important precursor of graphene since GO is highly dispersible in water and polar organic solvents and can be easily reduced into graphene.[13−19] Consequently, various polymer−graphene composites have been accessed by solution-processing approach on the basis of GO.[20−24] In addition, GO is made from graphite, which is abundantly available (the global graphite reserves are thought to be around 77 million tons;[25] the annual output of synthetic graphite reached an estimated 1.5 million tons[26]). All these merits of GO make its large-scale production and resultant graphene-based materials viable and sustainable.

Recently, our group found that GO can form nematic and lamellar liquid crystals (LCs) in water and polar organic solvents.[27] For the GO sheets with narrow distribution in lateral size, chiral liquid crystal (CLC) phase was even disclosed with both lamellar and helical features.[28] The discovery of GO LCs paves the way to highly ordered, macroscopic assembled graphene materials.[29−32] In particular, continuous neat graphene fibers, a novel kind of high-performance carbonaceous fibers, have been achieved by wet-spinning GO LCs.[28] The graphene fibers exhibited multifunctional attributes such as high mechanical strength, excellent flexibility, and fine conductivity.[33−35] Such a LC wet-spinning assembly strategy has been recently extended to fabricate nacre-mimetic fibers with building blocks of polymer-functionalized graphene.[36−39] The nacre-mimetic composites also showed good mechanical strength (158−200 MPa) and excellent flexibility (∼1−3% of strain) superior to nacre because of their fine "brick-and-mortar" (B&M) microstructures. Nevertheless, the LC phases of polymer-grafted GO or graphene have never been investigated and confirmed. Besides, the mechanical strength of graphene-based biomimetic fibers and films[40−44] is still much lower than those of Al_2O_3−chitosan (315 MPa)[45] and cross-linked montmorillonite−poly(vinyl alcohol) (MTM−PVA) (400 MPa)[46] composites. Thus, to make stronger biomimetic composites based on graphene and polymers is still a challenge.

Given the ultrahigh mechanical strength (∼130 GPa) of single graphene sheet,[47,48] stronger biomimetic composites should be accessible if greater interactions between graphene sheets were introduced.[49] Accordingly, we first synthesized polyacrylonitrile-grafted GO (GO-*g*-PAN) sheets by *in situ* free radical polymerization strategy in this article. The GO-*g*-PAN sheets were highly dispersible in polar organic solvents, forming nematic LCs at a low concentration. Upon increasing the concentration, GO-*g*-PAN evolved into lamellar LC phase.

Received: April 2, 2013
Revised: July 28, 2013
Published: August 21, 2013

ACS Publications © 2013 American Chemical Society

Scheme 1. Schematic Protocol To Synthesize GO-*g*-PAN and Make Bio-mimetic Fibers[a]

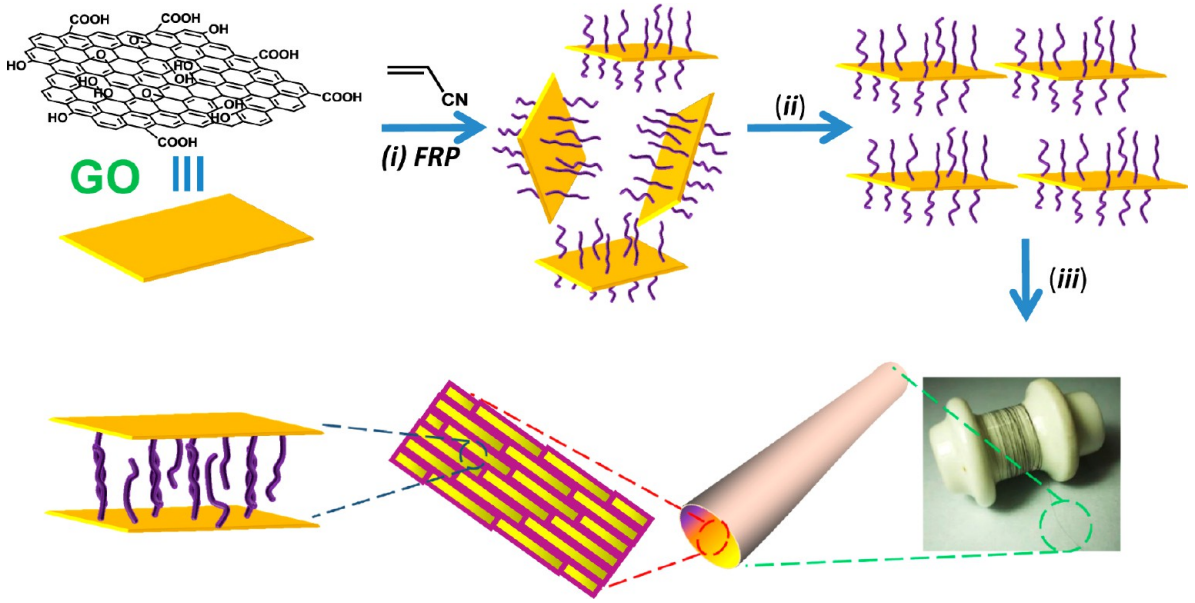

[a](i) Synthesis of GO-*g*-PAN building blocks by *in situ* free radical polymerization of acrylonitrile at 65 °C for 48 h in the presence of GO, followed by repeated centrifugation and DMF washing. (ii) Prealignment of GO-*g*-PAN in lamellar phase in DMF. (iii) Formation of hierarchically assembled continuous GO-*g*-PAN fibers via wet-spinning, and the supramolecular fibers possessing nacre-mimetic B&M microstructures are assembled from aligned GO-*g*-PAN building blocks.

Table 1. Selected Results of GO-*g*-PAN with Various Feed Ratio of Acrylonitrile to Initiator (*R*)

sample	*R*	M_n[a] (kDa)	PDI[b]	PAN content[c] (wt %)	height[d] (nm)	[C]/[O][e]	zeta-potential[f](eV)	av arm density[g] (chains/μm^2)
GO-*g*-PAN1	500:1	23.0	1.66	13.7	1.7	2.89	−27.7 ± 1.43	1599
GO-*g*-PAN2	1000:1	32.8	1.69	18.3	2.7	2.95	−25.3 ± 0.75	1589
GO-*g*-PAN3	2000:1	55.8	1.77	25.8	3.7	2.9	−22.6 ± 0.2	1425

[a]Number-average molecular weight of isolated PAN. [b]Polydispersity index of isolated PAN. [c]PAN content calculated by XPS. [d]Average height of polymer clusters on GO surfaces obtained from corresponding AFM images. [e]Molar ratio of carbon to oxygen atoms ([C]/[O]) excluding the carbon content of PAN. [f]Zeta-potential of GO-*g*-PAN dispersed in DMF. [g]Average density of the grafted PAN chains on GO with the unit of chains per μm^2.

Interestingly, CLC phase with both long-range lamellar and helical characters was found in the GO-*g*-PAN system, which is the first example in the field of polymer brush LCs. Continuous and tough nacre-mimetic fibers were made from GO-*g*-PAN LCs via the wet-spinning process. The fibers showed a tensile strength up to 452 MPa, the highest value for nacre-mimetic composites constructed with 2D platelets and polymers.

EXPERIMENTAL SECTION

Materials. Acrylonitrile (AN) was dried over calcium chloride for 48 h, distilled under reduced pressure, and stored at −20 °C. 2,2′-Azobis(2-methylpropionitrile) (AIBN) and potassium persulfate ($K_2S_2O_8$) were employed after twice recrystallization. Graphite powder (40 μm) was obtained from Qingdao Henglide Graphite Co., Ltd. Concentrated H_2SO_4 (98%) and $KMnO_4$ were purchased from Shanghai Reagents Company and used as received. GO was prepared from natural graphite powder according to a modified Hummers method reported previously.[50−52]

Synthesis of GO-*g*-PAN. PAN was grafted onto GO via the *in situ* free radical polymerization protocol established by our group previously (Scheme 1i).[53,54] Typically, 100 mg of GO and 80 mL of dimethylformamide (DMF) were added to a 150 mL round-bottom flask, and a well-dispersed solution was obtained by sonicating in a 40 kHz sonic bath for 10 min. Followed by addition of 10.6 g of AN (200 mmol) and 82 mg of initiator of AIBN (0.5 mmol), the solution was purged with nitrogen for 40 min and then immersed in an oil bath at 65 °C. After reacting for 48 h under N_2 protection and stirring, the reaction was terminated by exposure to air. The resultant mixture was precipitated in methanol, and the resulting gray precipitate was collected and redissolved in 200 mL of DMF. The solution was then centrifuged at the speed of 15 000 rpm (23 300*g*) for 0.5−1 h to remove free polymers that did not covalently attached to GO. The resultant cream-like gel was thoroughly washed with DMF for at least eight times until the upper layer appeared colorless. Then the resulting black colloidal product of GO-*g*-PAN was dispersed in 50 mL of DMF ready for use.

Macroscopic Assembly of Fibers and Papers. The GO-*g*-PAN fibers were made by the wet-spinning assembly approach with a coagulation bath of methanol, similar to our previous protocol to fabricate neat graphene fibers (Scheme 1iii).[36−39] The GO-*g*-PAN dispersed in DMF was concentrated to 30−40 mg/mL by centrifugation treatment and then transferred into a syringe. The concentrated GO-*g*-PAN colloidal dispersion with helical lamellar structure was squeezed through a spinneret into the coagulation bath at a rate of 125 μL/min (about 0.5 m/min) at room temperature. After 30 s immersion in methanol, the fibers were collected onto the drum. The wet fibers were dried at room temperature in air for 30 min and then dried at 50 °C under vacuum for 12 h to give the final macroscopic assembled fibers. We obtained three samples of GO-*g*-PAN, designated as GO-*g*-PAN1, GO-*g*-PAN2, and GO-*g*-PAN3, by adjusting the feed ratio of monomer to initiator (*R*). The reaction conditions and selected results are shown in Table 1.

The GO/PAN3 blending composite was prepared by solvent blending of GO and PAN3 isolated from the polymerization system with the PAN3 content of 25.8 wt %. The DMF/methanol mixtures

dx.doi.org/10.1021/ma400681v | *Macromolecules* 2013, 46, 6931−6941

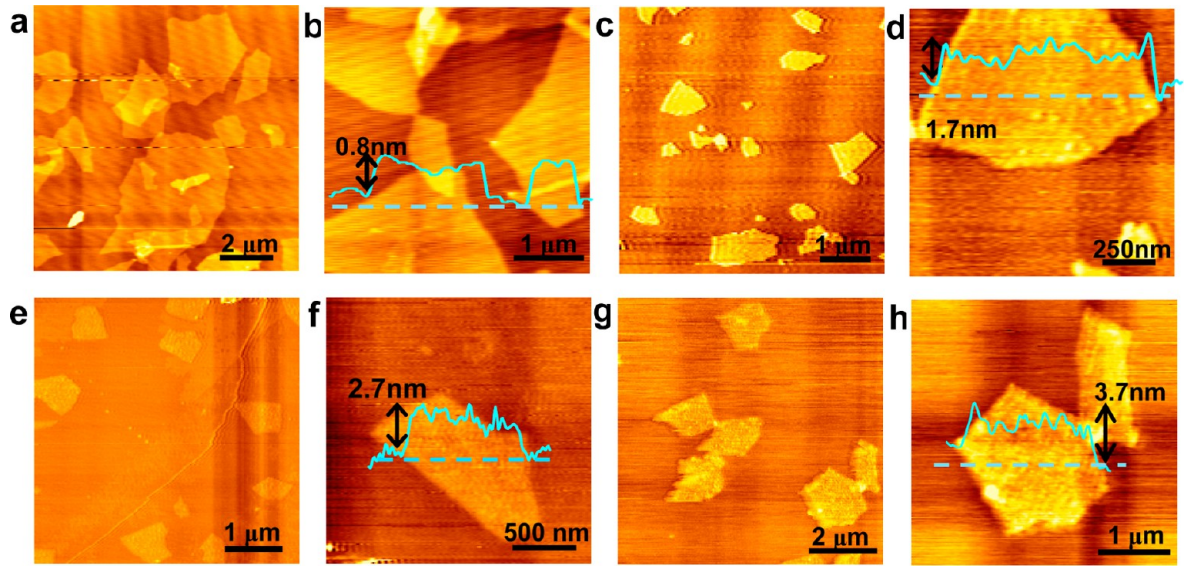

Figure 1. AFM images of (a, b) pristine GO, (c, d) GO-*g*-PAN1, (e, f) GO-*g*-PAN2, and (g, h) GO-*g*-PAN3.

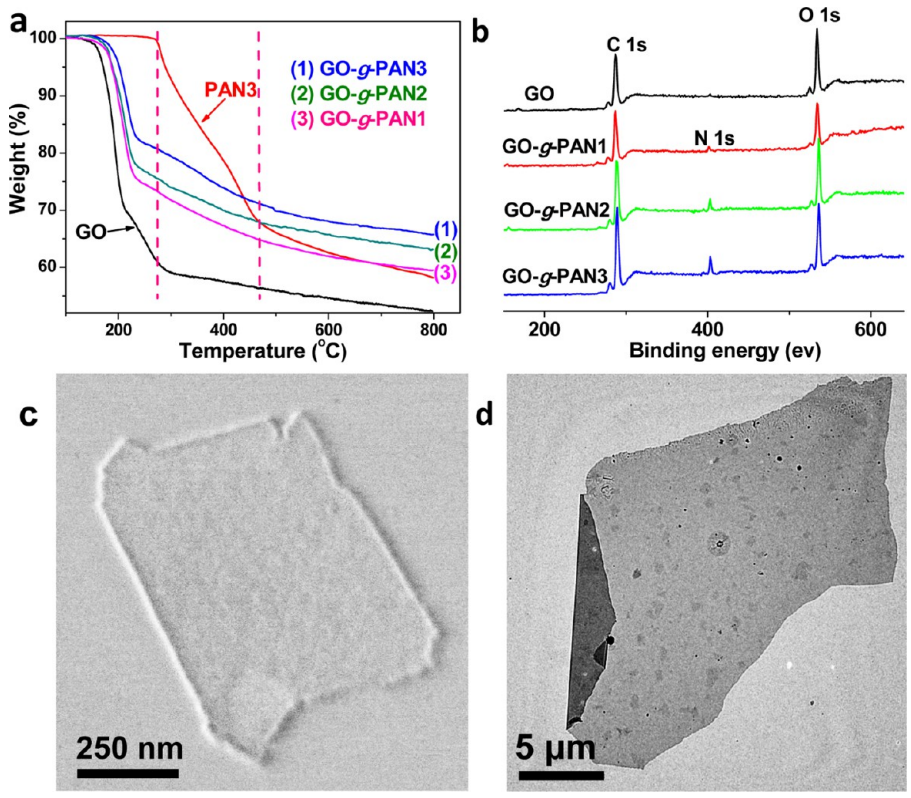

Figure 2. (a) TGA curves for samples of neat PAN3, GO, and GO-*g*-PANs. (b) XPS spectra of GO and GO-*g*-PANs. Representative SEM (c) and TEM (d) image of single-layer GO-*g*-PAN3.

were used as coagulation bath for GO/PAN blending fibers. The paper of GO-*g*-PAN was prepared by vacuum-assisted filtration of DMF dispersion with concentration of 5 mg/mL, followed by drying at 50 °C in vacuum for 12 h. The density of GO-*g*-PAN3 paper is 1.72 g/cm^3, as calculated by the weight divided by the volume.

Characterization. Atomic force microscopy (AFM) characterization was performed on a NSK SPI3800 under tapping mode with samples prepared by spin-coating onto freshly peeled mica substrates at 1200 rpm from diluted sample solutions. Thermal gravimetric analysis (TGA) was done in a TGA PYRIS6 equipment from PE, using a heating rate of 10 °C/min in a nitrogen atmosphere. Fourier-transform infrared (FTIR) measurements were done on a Bruker Vector 22 spectrometer (KBr disk). Transmission electron microscopy (TEM) analysis was performed on a JEOL JEM1200EX electron microscope at 120 kV. Scanning electron microscopy (SEM) images were performed on a Hitachi S4800 field emission SEM system. The X-ray diffraction (XRD) measurements were taken on a Philips X'Pert PRO diffractometer equipped with Cu KR radiation (40 kV, 40 mA) with an X-ray wavelength (λ) of 1.5418 Å. X-ray photoelectron spectroscopy (XPS) was performed using a PHI 5000C ESCA system operated at 14.0 kV. All binding energies were referenced to the C 1s neutral carbon peak at 284.8 eV. Absorption spectra were recorded at room temperature on a Varian Cary 300 Bio UV–vis spectrophotometer. The measurement of zeta potential was carried out on a

dx.doi.org/10.1021/ma400681v | *Macromolecules* 2013, 46, 6931–6941

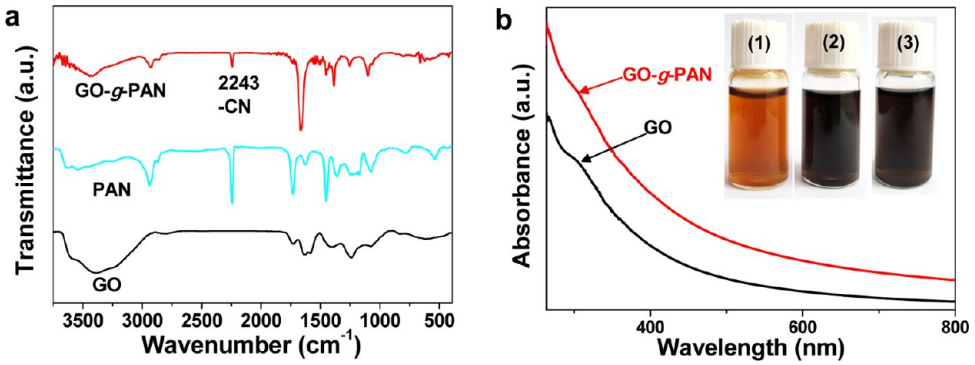

Figure 3. (a) FTIR spectra of GO-*g*-PAN, PAN, and GO. (b) UV−vis spectra of 0.5 mg/mL GO and GO-*g*-PAN3 dispersed in DMF. Inset: GO dispersed in DMF (1); GO-*g*-PAN dispersed in DMF (2) and DMSO (3).

Malvern ZET-3000HS apparatus. Polarized optical microscopy (POM) observations were performed using a Nikon E600POL, and the liquid samples were loaded into the planar cells. Small-angle X-ray scattering (SAXS) tests were carried out at Shanghai Synchrotron Radiation Facility (SSRF), by using a fixed wavelength of 0.124 nm, a sample-to-detector distance of 5 m, and an exposure time of 300 s. The scattering patterns were collected on a CCD camera, and the curve intensity vs q was obtained by integrating the data from the patterns. Circular dichroism (CD) spectra were collected on a Bio-Logic MOS-450 spectrometer, and the samples were injected into the cell with a thickness of 0.2 cm. The tensile tests were carried out on a HS-3002C mechanical testing system. Both ends of individual fibers were attached onto clamps by a piece of tape and then clamped. A loading rate of 2 mm/min was applied in all the tests. The cross-section area was determined from SEM images of fracture section.

RESULTS

Characterization of GO-*g*-PAN. Scheme 1i shows the synthesis protocol of GO-*g*-PAN by *in situ* free radical polymerization. The preparation process is very simple, and the raw materials including GO and monomer could be commercially available, facilitating the scalable production and application of GO-*g*-PAN.[55,56] Notably, polymers were only partially grafted on GO surfaces during the polymerization, and the ungrafted free polymers were completely removed from the resulting samples of GO-*g*-PAN by repeated washing and centrifugation. Consequently, we focus on the fluid behavior and macroscopic assembly of neat polymer-grafted GO sheets (also called 2D macromolecular brushes) in this article, rather than the composite system of GO-*g*-PAN and polymer. Figure 1 shows the AFM images of GO and GO-*g*-PAN. The average heights of GO-*g*-PAN increased from ∼0.8 nm for pristine GO to 1.7 nm for GO-*g*-PAN1 (Figure 1c,d), 2.7 nm for GO-*g*-PAN2 (Figure 1e,f), and 3.7 nm for GO-*g*-PAN3 (Figure 1g,h), as the corresponding feed ratio (R) of monomer to initiator varied from 500/1 to 1000/1 to 2000/1, respectively. Compared with the flat surface morphology of pristine GO, various protuberances, tufts of polymeric hairs, are evenly distributed on the whole sheets of GO-*g*-PAN, and the height of GO-*g*-PAN increased gradually with increasing R, indicating the efficient covalent grafting of PAN on the surfaces of GO. The GPC trace of free PAN isolated from the reaction system also reflects the increasing of number-averaged molecular weight (M_n) upon R (see Table 1 and Figure S1).

We also checked the polymer grafting by TGA measurements. Figure 2a shows the weight loss curves of GO, isolated neat PAN3, and GO-*g*-PANs. The main weight loss below 250 °C is due to the decomposition of the oxygen-containing functional groups of GO. It is suggesting that labile functional groups of GO were partially decomposed during the radical polymerization process. The weight loss curves of GO-*g*-PANs indicate that the grafted PAN content increases with increasing R. Obvious mass loss steps of PAN can be observed in the curves of GO-*g*-PANs. The onset of PAN decomposition is at 271 °C in GO-*g*-PANs, whereas in PAN3 the onset of decomposition is at 237.5 °C. During thermal treatment, the pure PAN would experience interchain cyclization reactions,[57,58] which explains the 59% residual weight of PAN3. When it comes to PAN grafted GO, the reactions of PAN and GO would be complex. Therefore, the quantities of grafted PAN were not determined by TGA in this study. Despite this deviation in quantitative expression of TGA, the weight loss tendency of GO-*g*-PANs is consistent with the increase of thickness of grafted sheets.

The quantitative element compositions of GO-*g*-PAN were measured by XPS (Figure 2b). Both C 1s (∼285 eV) and O 1s (∼531 eV) signals were detected for both GO and GO-*g*-PAN, and as expected, the N 1s (∼398 eV) signal was only detected for the GO-*g*-PAN samples. The nitrogen contents of GO-*g*-PAN1, GO-*g*-PAN2, and GO-*g*-PAN3 are 3.3, 4.4, and 6.2 at. %, respectively. Accordingly, the PAN fractions in the GO-*g*-PAN were estimated to be 13.8, 18.5, and 25.8 wt %. The calculated average densities of the grafted PAN chains on a single side of GO are 1599, 1589, and 1425 chains per μm^2 ($d_2 = K_2(W_P/W_C)$, wherein $K_2 = 4.58 \times 10^3$, W_P and W_C the weight fractions of GO backbone and grafted polymer, respectively).[53] In addition, the pristine GO had a molar ratio of carbon to oxygen atoms ([C]/[O]) of 2.23, whereas the samples of GO-*g*-PAN showed higher values of [C]/[O] (2.89−2.95) even excluding the carbon content of PAN. This was also attributed to the partial reduction of GO during the polymerization process.

Figure 2c,d shows the representative SEM and TEM images of individual sheet of GO-*g*-PAN3. From SEM observation (Figure 2c), we can find that the flat surface is coated with a rough polymer layer. The existence of PAN on the planar sheet is also confirmed by TEM observation, showing that GO sheet was evenly decorated with polymer clusters, as indicated by the relatively darker points on the GO sheet (Figure 2d).

In the FTIR spectra of GO, PAN, and GO-*g*-PAN (Figure 3a), the characteristic peaks of GO including the C═O groups stretching vibration at 1720 cm^{-1} and the strong aromatic carbon double bonds at 1630 cm^{-1} were observed before and after the functionalization with PAN chains.[59,60] The spectrum of GO-*g*-PAN shows a distinct absorption band at 2243 cm^{-1} attributed to the −CN group of PAN, and strong peaks at 2939,

dx.doi.org/10.1021/ma400681v | *Macromolecules* 2013, 46, 6931−6941

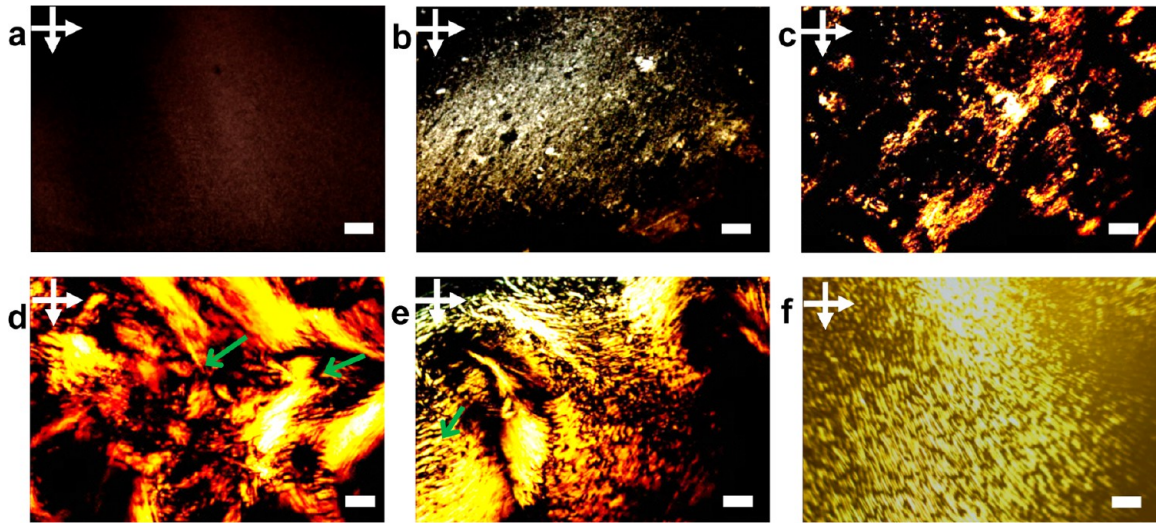

Figure 4. (a–f) POM images between crossed polarizers of GO-*g*-PAN3 DMF dispersions in planar cells with ϕ of 0.035%, 0.23%, 0.47%, 0.52%, 0.69%, and 1.16% (from a to f). The green arrows indicate the disclinations in (d) and lamellar phases in (f), and the scale bars are 200 μm.

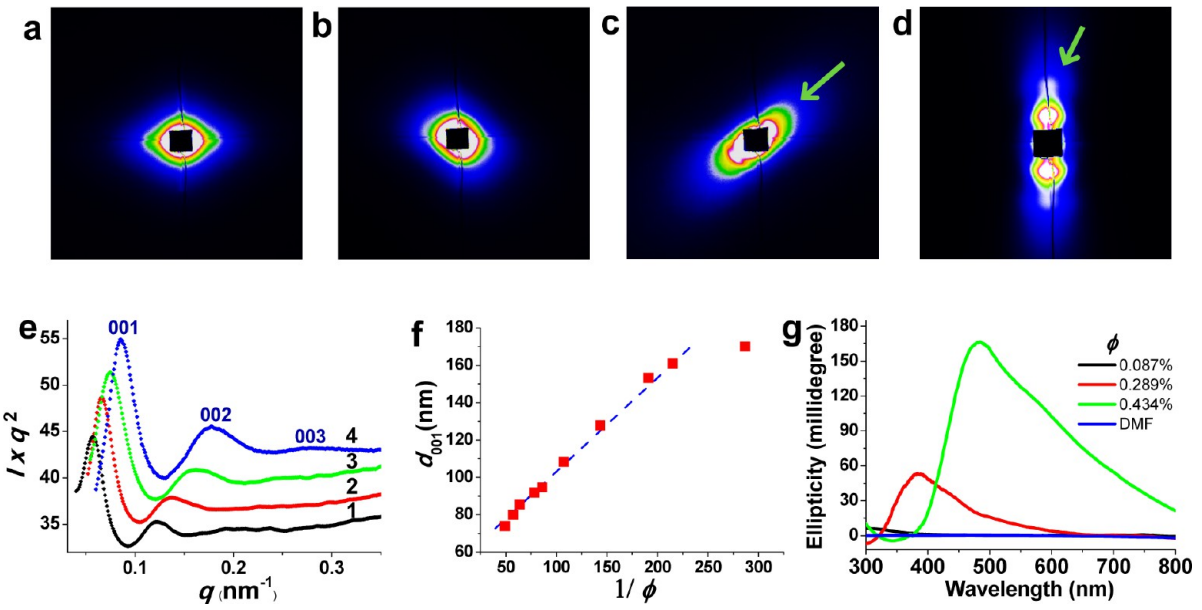

Figure 5. (a–d) 2D scattering patterns of GO-*g*-PAN dispersed in DMF with successive volume fractions (ϕ) of 0.52, 1.16, 1.74, and 2.04%. The diffusive arcs (arrows) in (c) and (d) denote the reflection arcs. (e) Profiles of scattering intensity as a function of scattering vector q ($q = 4\pi \sin \theta/\lambda = 2\pi/d$) in samples with successive ϕ of 0.52, 1.16, 1.74, and 2.04% (successively numbered by 1–4). (f) Correlation of d (001) spacing and $1/\phi$; the red squares are experimental values, and the blue line is the fitting function in the linear region ($\phi \geq 0.5\%$). (g) CD spectra of GO-*g*-PAN3 CLCs dispersions and neat DMF.

1454, and 1360 cm^{-1} could be assigned to C–H stretching vibration and C–H bending vibration in CH_2 and CH of PAN backbones, respectively, indicating the introduction of PAN chains onto GO sheets.[61,62]

Just like pure PAN, the GO-*g*-PAN sheets have good dispersibility in DMF and dimethyl sulfoxide (DMSO) (Figure 3b), paving the way to continuous solution-processing. The GO-*g*-PAN solution became into deep brown from the light brown of pristine GO, mainly due to the partial reduction (Figure 3b). This was also identified by the UV–vis absorption spectra. Compared with GO, the absorption of GO-*g*-PAN in the whole wavelength range increased due to the reduction, and the shoulder assigned to the absorption of carbonyl bond between 300 and 400 nm decreased relative to the aromatic bond absorption at 280–300 nm (Figure 3b).

Liquid Crystal of GO-*g*-PAN. Pristine GO can form nematic, lamellar, and chiral liquid crystal phases in water.[27,28] Can polymer-grafted GO sheets also form rich liquid crystal (LC) phases? To answer this question, the DMF dispersions of GO-*g*-PAN (representative sample of GO-*g*-PAN3) at various concentrations were first observed by POM. The evolved birefringence between crossed polarizers upon the concentration is the direct proof of lyotropic LCs (Figure 4a–f). With increasing concentrations, the evolutions of mesophases were observed: (1) isolated birefringence domains appear as the volume fraction of GO-*g*-PAN (ϕ) rose to 0.23% (Figure 4b), implying the start of the isotropic–nematic (I–N) phase transition; (2) upon increasing ϕ to 0.47%, stable birefringent suspensions extended to the whole region with Schlieren texture (Figure 4c), a typical feature for nematic phase;(3) as ϕ

dx.doi.org/10.1021/ma400681v | *Macromolecules* 2013, 46, 6931–6941

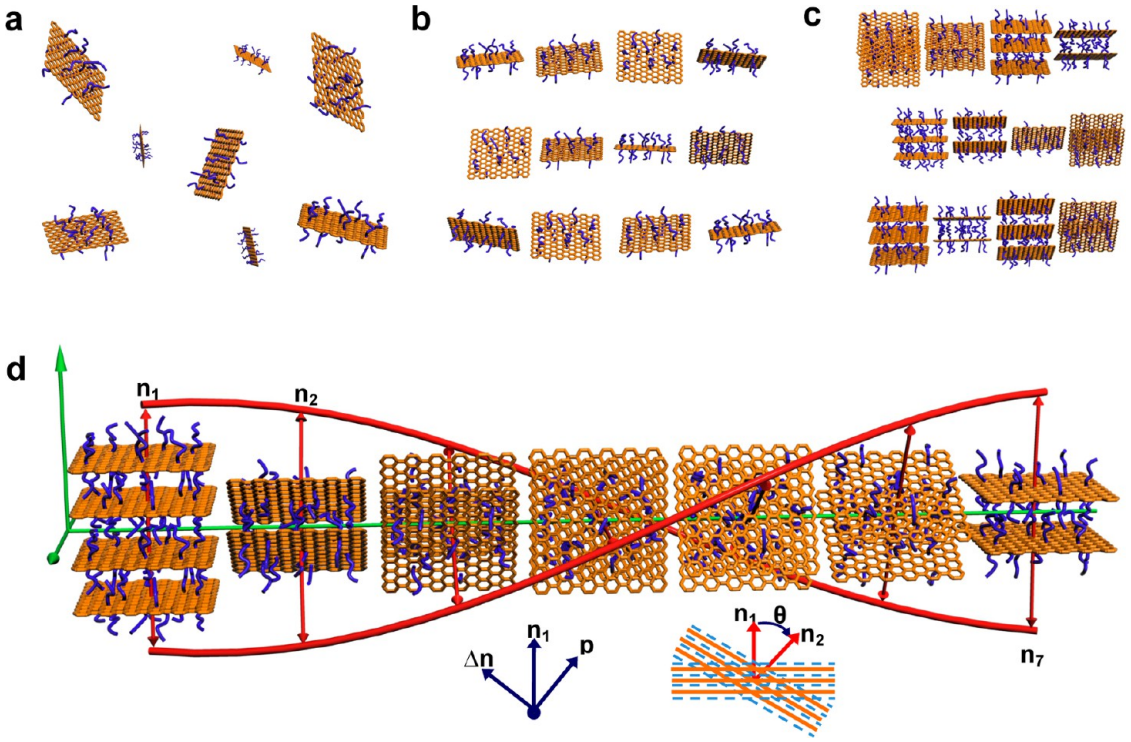

Figure 6. Evolution of isotropic (a), chiral nematic (b), the intermediate state between chiral nematic phase and helical lamellar phase (c), and one pitch (d) of helical lamellar phase for GO-*g*-PAN dispersions in DMF. The blue strings indicate grafted PAN chains, and GO sheets are simplified as yellow meshes. GO-*g*-PAN sheets randomly distribute in isotropic phase, align with an orientation vector (n) perpendicular to the sheet planes with a small portion of partial helix in the nematic phase, and the lamellar blocks rotate anticlockwise along the helical axis with the vectors (n_s) in the lamellar phase.

approached 0.52%, the existence of large area of Schlieren textures indicated uniform orientational ordering (Figure 4d), and singularities at the center of two-armed brushes corresponding to the disclinations in the ordered LC structures were observed simultaneously; (4) at higher concentration (e.g., ϕ = 1.16%), birefringent gels with parallel-banded structures formed (Figure 4f), implying the LC evolved into more ordered lamellar mesophase. Such evolutions of GO-*g*-PAN LC are quite similar to those of narrow-distributed pristine GO sheets.[28]

We further investigated the quantitative structural information on the evolution of LCs with SAXS measurements. Generally, a chaotic distribution was observed in the I phase of dilute dispersions, while ordered alignments were found in the concentrated N phase favoring orientation vectors.[63] In the isotropic state, the X-ray scattering intensity (In) of dilute GO-*g*-PAN3 suspensions (e.g., ϕ = 0.035%) showed monotonous and exponential decrease as a function of scattering vector modulus (q) with a factor of −1.75 ($In \sim q^{-1.75}$). Such a factor is close to the theoretical value (−2) for the ideal 2D planar colloids,[64] proving the flat morphology of GO-*g*-PAN3 dispersed in DMF. At higher volume concentrations (e.g., 0.23−0.47%), typical 2D elliptical SAXS diffusive patterns of nematic phase were observed, displaying interior anisotropic alignments. Besides, the appearance of a sharp scattering peak also confirmed the sole orientational order under this state. For concentrated dispersions above the I−N transition (e.g., $\phi \geq$ 0.7%), the GO-*g*-PAN3 samples exhibited strong anisotropy patterns (Figure 5c,d) and multiple correlation peaks (up to 3), corresponding to the lamellar phase observed in POM (Figure 4f). The detailed information on lamellar orders depending on GO-*g*-PAN concentration is revealed by the profiles of scattering intensity vs scattering vector (Figure 5e). Since the q ratio of three peaks is around 1:2:3, the highest peak (q_0) can be indexed to the 001 reflection of the lamellar structures.

The evolution of the interlayer spacing ($d = 2\pi/q_0$) for the GO-*g*-PAN sheets in DMF as a function of inverse volume fraction ($1/\phi$) provides more information on the local lamellar ordering of the suspensions (Figure 5f, the detailed data see Figure S4). At the range of ϕ 0.47−2.04%, the evolution displays a linear relation, where d is proportional to $1/\phi$ ($d = t/\phi$, t is the thickness of GO-*g*-PAN), representing the one-dimensional swelling behavior of lamellar 2D colloids LCs.[64] The dashed straight fitting line slope shown in Figure 5f is 0.53 ± 0.01 nm, reflecting the thickness of GO-*g*-PAN3 sheets calculated from the SAXS data. For $\phi \leq$ 0.35%, linear region ends as d levels off and reaches a maximum, where both lamellar and nematic phase textures were observed in POM investigations (Figure 4d). For diluted dispersions with lower ϕ, d value is deviated from the first linear region, which possibly corresponds to the 1-dimensional (1D) isotropic volumes swelling behavior in the nematic phase.[47,48]

It was found that GO LCs were mainly stabilized by the electrostatic repulsion of GO sheets due to their plenty of polar and charged functional groups.[27,28] As a polar organic solvent, DMF has strong interaction with graphene for the dipole−induced dipole interactions. To evaluate the possible electrostatic repulsion between GO-*g*-PAN sheets in DMF, we measured their zeta potential in DMF, as listed in Table 1. The zeta potential of pristine GO was −32 ± 0.76 mV; it decreased from −27.7 ± 1.43 to −22.6 ± 0.2 mV with the increasing molecular weight of grafted PAN chains. This

dx.doi.org/10.1021/ma400681v | *Macromolecules* 2013, 46, 6931−6941

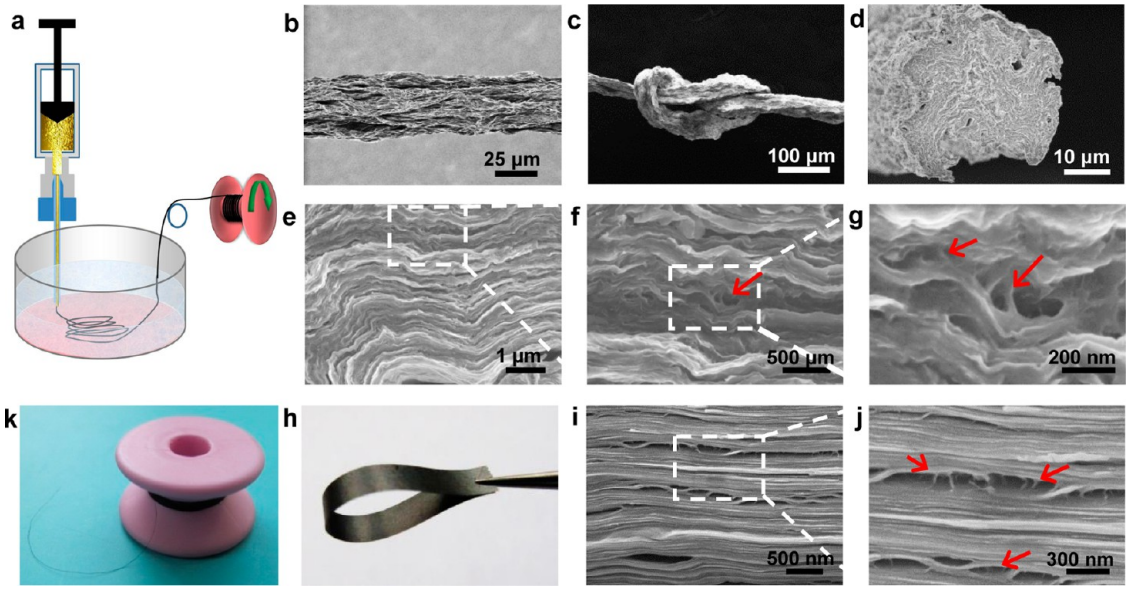

Figure 7. (a) Schematic apparatus for spinning GO-*g*-PAN fibers. The surface winkled morphology (b) and the knot (c) of GO-*g*-PAN3 fibers. (d–g) SEM images of section morphology of GO-*g*-PAN3 fiber. (h) A free-standing paper of GO-*g*-PAN3. (i, j) SEM images of section morphology of GO-*g*-PAN3 paper. (k) A 5 m long GO-*g*-PAN3 fiber wound on a ceramic reel.

implies that the grafting of PAN slightly decreases the surface charges of GO, which is ascribed to the partial reducing of GO during polymerization process. So we speculate that the remained charges on GO-*g*-PAN sheets and the free-volume entropic repulsion of grafted brush-like polymers are the main factors for the delicate balance of GO-*g*-PAN LCs.[65]

GO-*g*-PAN CLCs. In liquid crystals area, the chiral mesophases can be defined by the broken rotational symmetry of the direct vectors of constituent mesogenic units. To date, the chiral liquid crystal family includes the general mesophases originated from chiral molecular structures (e.g., the well-established cholesteric phases)[66] and chiral phases organized from achiral molecules (e.g., polar LCs of banana-shaped molecules).[67] Recently, our group found that the aqueous LCs of GO behaved as a chiral liquid crystal phase with lamellar structure.[28] Here, we examined the GO-*g*-PAN dispersion of DMF and found the similar chiral lamellar behavior to GO CLCs.

As shown in Figure 4d–f, fingerprint-like textures were observed under POM for GO-*g*-PAN DMF dispersions at the concentration above 0.52%, implying the existence of helical or chiral structures in such a lamellar ordering.[68,69] We also measured CD spectra of GO-*g*-PAN DMF dispersions and found that the CD signal of the GO-*g*-PAN LC becomes stronger and wider upon increasing concentration, indicating the gradual formation of helical configuration for the polymer-functionalized GO sheets (Figure 5g). At ϕ = 0.43%, very strong CD signal up to 166 mdeg was detected. Moreover, the characteristic CD spectrum spans from 300 to 800 nm that covers a wide range from near-ultraviolet and visible light to near-infrared, revealing a gradient helical arrangement of GO-*g*-PAN sheets.[28]

Evolution of GO-*g*-PAN CLCs. According to the aforementioned observations and measurements, we tried to understand the GO-*g*-PAN CLCs.[28] The evolution of GO-*g*-PAN CLCs originated from isotropic dispersions, as depicted in Figure 6. Upon increasing ϕ, isotropic dispersions (Figure 6a) transform into nematic phase with orientation of GO-*g*-PAN sheets, and twisted configuration also forms at local domains simultaneously due to the repulsion between grain boundaries of closed sheets (Figure 6b). At higher concentrations, the twisted configuration gradually develops into more ordered helical structures, and helical lamellar phase starts to appear because of the volume and charge repulsions among GO-*g*-PAN sheets (Figure 6c). In a concentrated dispersion, the nematic phase transforms completely into lamellar phase, resulting in long-range ordered structures with both well-defined lamellar and helical characters (Figure 6d). Such a new mesophase of CLCs needs more theoretical and experimental works to be fully understood.

Estimation of Correlation Lengths for GO-*g*-PAN LCs. In this article, we prepared GO-*g*-PAN and for the first time disclosed its CLC phase in DMF. Such ordered system in fluid could be quantitatively analyzed according to the SAXS results shown in Figure 5 in terms of thermal fluctuation and correlation length (ξ, for the distance longer than ξ, the layer height fluctuations are coherent from layer to layer, whereas for distance smaller than ξ, fluctuations are single layer and incoherent).[70] According to the Landau–Peierls argument[71] and the P. G. de Gennes theory,[72] the thermal fluctuation in smectic (lamellar) phases can be calculated by Callié analysis.[73] The quasi-long-range order of Landau–Peierls instability in the neat GO CLC system was previously analyzed by our group,[28] with eqs 1 and 2:

$$\eta = q_0^2 k_B T/8\pi(BK)^{1/2} \quad (1)$$

$$\xi = (Kd^2/B)^{1/4} \quad (2)$$

where k_B is the Boltzmann constant (1.38×10^{-23} J K^{-1}), B the bulk compression modulus (erg/cm^3), T the thermodynamic temperature (298 K), K the restoring force of LC suspensions, and ξ a correlation length for the fluctuation. Here we also used the same equations to speculate the correlation lengths of GO-*g*-PAN CLC suspensions. K could be roughly calculated by multiplying the elastic modulus (E, ~0.25 TPa for GO)[74] by the average sheet area of GO-*g*-PAN (0.548 ± 0.31 μm^2). It is

dx.doi.org/10.1021/ma400681v | *Macromolecules* 2013, 46, 6931–6941

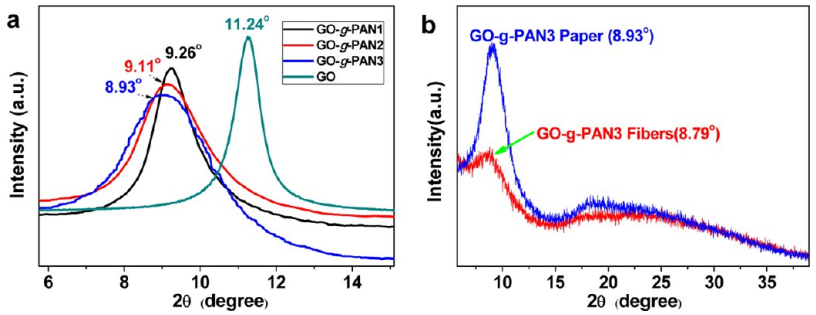

Figure 8. (a) XRD patterns of GO-*g*-PANs and GO papers. (b) XRD patterns of GO-*g*-PAN3 fibers and papers.

$(1.37 \pm 0.78) \times 10^{-4}$ N, about 8 orders of magnitude larger than that of a conventional smectic phase of organic small molecules ($\sim 10^{-12}$ N).[75,76] Such a giant K value implies that the GO-*g*-PAN sheets were hard to deform.

On the other hand, K, is also called as Frank elastic constant of single GO-*g*-PAN sheet in suspensions, which could be obtained from eq 3 that derived from standard beam bending equations.[77]

$$K = \phi E t^2/12 \tag{3}$$

where K denotes the Frank elastic constant, t the thickness of sheet (0.989 nm), E the elastic modulus of GO (0.25 TPa), and ϕ the sheet volume fraction in the suspensions. The calculated K values (1.06×10^{-10}–4.16×10^{-10} N) of GO-*g*-PAN CLCs suspensions were much closer to an elastic value of GO estimated by simulation ($\sim 10^{-10}$ N)[78] and a typical nematic elastic constant of small molecules ($\sim 10^{-12}$ N).[79,80] The calculated ξs of our GO-*g*-PAN CLCs are ranging from 5.25 ± 0.2 to 7.86 ± 0.4 μm. The ξ values are around 3 orders of magnitude higher than that in the conventional smectic phase of small molecules,[81] implying the little thermal fluctuation in GO-*g*-PAN CLCs. This feature mainly originated from the rigid, solid-like structure of individual graphene sheets. Similar results were reported previously in the 2D system of lyotropic phosphatoantimonate LC,[82] zirconium phosphate platelets,[83] and poly(*N*-isopropylacrylamide)−clay nanocomposites.[84,85]

Continuous Assembly of Nacre-Mimetic Fibers Micrometer in Diameter. The long-range orientation in the lamellar phase of GO-*g*-PAN dispersions allows for macroscopic assembly of ordered structures. For producing continuous GO-*g*-PAN fibers, the GO-*g*-PAN suspensions of 35 mg/mL were injected through the spinneret (100 μm inner diameter) into the methanol coagulation bath (Figure 7a). Compared to sodium, potassium, or calcium salt solutions of coagulation bath for wet-spinning assembly of GO fibers,[86] methanol was employed as coagulation bath in this study due to the PAN grafting, which simplifies the spinning process and avoids the staining of metallic salts to the resultant fibers. After 30 s of coagulation, continuous GO-*g*-PAN fibers were collected onto the drum. The diameters of fibers further shrunk to around 25 μm in 1 min during the collection owing to the fast evaporation of methanol (Figure 7d). The small diameters of fibers would greatly minimize defects and further increase the fiber strength.[87−91] From the concentrated GO-*g*-PAN colloidal gel, we obtained meters of continuous fibers within 20 min (Figure 7k). A knot was tied without breakage (Figure 7c), signifying the flexibility of neat GO-*g*-PAN fibers. The surface of fibers shows the uniform orientation of GO-*g*-PAN sheets along the fiber axis, demonstrating efficient alignment of GO-*g*-PAN sheets during the wet-spinning process for fiber production (Figure 7b). The low-magnification SEM image shows the cross section of a GO-*g*-PAN fiber (Figure 7d), and tightly packed layered structures are observed. It implies that GO-*g*-PAN sheets strongly adhere with each other based on the prealignment of GO-*g*-PAN LCs. Highly ordered lamellar structures with rolling wrinkles are observed from the magnified SEM image of local fiber cross section (Figure 7e). The soft interlayer of PAN grafts is clearly observed from the largely magnified SEM image, especially at the exfoliated fracture domains as marked by the arrows (Figure 7f,g), well revealing the bridging role of PAN between neighbored graphene sheets. This resembles the classic "brick-and-mortar" (B&M) structure widely expressed in nacre of natural sea-shell and other biomimetic composites.[41−44] In our case, notably, polymer chains are covalently immobilized on the rigid "brick" of graphene sheets, so there is no obvious phase interface between "brick" and "mortar", which would enhance the mechanical performance of composites. On the contrary, clear phase interface is generally existed between the "brick" of inorganic platelets and "mortar" of polymers in previous biomimics because of their noncovalent interactions. As a comparison, GO-*g*-PAN papers were also prepared via the vacuum-assisted filtration assembly protocol, exhibiting flattened, ordered lamellar microstructures (Figure 7i). Under a high magnification SEM image, fibrous polymers are also observed at the interlayer of graphene sheets (Figure 7j), confirming again the successful grafting of PAN on GO sheets.

The GO-*g*-PAN fibers and papers were further characterized by XRD (Figure 8). Because of the PAN grafting, the corresponding d-spacing between adjacent sheets, calculated from the 2θ degree ($d = \lambda/2 \sin \theta$), increased from 7.86 Å for neat GO paper to 9.89 Å for GO-*g*-PAN3 paper (Figure 8a). The GO-*g*-PAN3 fibers also exhibited a peak at 2θ 8.79° corresponding to the (001) interplanar spacing of 10.04 Å (Figure 8b). This reveals that the nacre-mimetic GO-*g*-PAN fibers preserved the ordered lamellar structures from the LC dopes during the wet-spinning process.

Mechanical Properties of Nacre-Mimetic GO-*g*-PAN Fibers. The hierarchically assembled structures and covalent linkage between polymer and graphene favor the mechanical performance of biomimetic fibers. Tensile tests on GO-*g*-PAN3 fibers revealed that the tensile strength (σ), Young's modulus (E), and ultimate strain (ε) were 452 ± 24 MPa, 8.31 ± 0.56 GPa, and 5.44 ± 0.34%, respectively (Figure 9). Fibers with lower PAN contents showed weaker mechanical properties (Table 2), which are 273 ± 17.5 MPa of σ, 5.76 ± 0.87 GPa of E, and 4.83 ± 0.28% of ε for GO-*g*-PAN2 fibers, whereas 150 ± 11 MPa of σ, 3.28 ± 0.63 GPa of E, and 4.56 ± 0.22% of ε for GO-*g*-PAN1 fibers. This could be attributed to the higher

dx.doi.org/10.1021/ma400681v | *Macromolecules* 2013, 46, 6931−6941

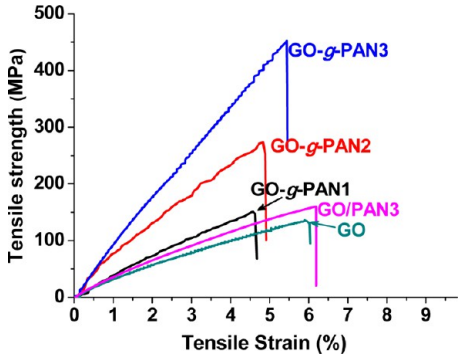

Figure 9. Typical mechanical measurements under tensile loading for GO-*g*-PAN fibers, neat GO fiber, and GO/PAN3 blending fiber.

Table 2. Mechanical Properties for Fibers Obtained by Tensile Testing

samples	ultimate stress (MPa)	Young's modulus (GPa)	ultimate strain (%)	toughness (J/cm^3)
GO-*g*-PAN1 fibers	150 ± 11	3.28 ± 0.63	4.56 ± 0.22	3.4
GO-*g*-PAN2 fibers	273 ± 17.5	5.67 ± 0.87	4.83 ± 0.28	6.6
GO-*g*-PAN3 fibers	452 ± 24	8.31 ± 0.56	5.44 ± 0.34	12.3
GO/PAN3 blending fibers	160 ± 10	2.59 ± 0.36	6.18 ± 0.42	4.9
neat PAN fibers	26 ± 4	3.43 ± 0.51	0.76 ± 0.14	0.099
neat GO fibers	136 ± 11.7	2.29 ± 0.21	5.9 ± 0.31	4.0

interaction between graphene sheets for the cases of higher polymer grafting.

For comparison, we also prepared neat PAN3 fibers, neat GO fibers, and blended fibers of PAN3 and GO under the comparative spinning conditions and measured their mechanical properties (Table 2). The GO-*g*-PAN3 fibers are about 2–3-fold stronger and 3–4 times stiffer than neat GO fibers and GO/PAN3 blending fibers while keeping the similar strain and more than 1 order of magnitude stronger than the neat PAN3 fibers. The control experiments further demonstrate that covalent grafting of polymers facilitates the significant improvement of mechanical property of nacre-mimetic composites.

The GO-*g*-PAN3 fibers are also much stronger than graphene-based composites reported previously which generally showed σs of 110–220 MPa (Figure 10).[92−97] Compared to nacre (σ 110–130 MPa, ε 1%),[40] our GO-*g*-PAN3 fibers displayed nearly 4 times higher strength and over 1 order of magnitude higher strain. Significantly, our GO-*g*-PAN3 fibers are even stronger than the artificial nacre composites of Al_2O_3–chitosan with covalent linkage (315 MPa)[45] and cross-linked MTM–PVA (400 MPa)[46] which are the record values reported in the past two decades.[41−44,98] Furthermore, since our nacre-mimetic fibers are strong and flexible, they also exhibited relatively high toughness (12.3 J/cm^3 in Table 2, Figure 10b), which is much greater than nacre (0.22 J/cm^3)[40,99] and general nacre-mimics (0.06–2 J/cm^3).[46,100]

CONCLUSIONS

In summary, we synthesized PAN-grafted GO (GO-*g*-PAN) via a simple method of *in situ* free radical polymerization. The resultant GO-*g*-PAN showed high dispersibility in polar organic solvents and thus formed lyotropic LCs above a very low critical concentration (0.23 vol %). With increasing concentration, GO-*g*-PAN suspensions in DMF displayed a complex evolution from nematic phase with sole orientation to chiral LC phase with both helical and lamellar structures. The estimated correlation length of the graphene-based LCs is much greater (2–4 orders of magnitude) than that of the LCs of small molecules, indicating the little thermal fluctuation in the giant 2D sheet suspensions. The discovery of helical lamellar phase at the system of polymer brushes enriches the LC fields of both polymers and colloids. Wet-spinning of the neat GO-*g*-PAN LCs gave birth to continuous nacre-mimetic fibers micrometer-scale in diameter. The tensile strength and Young's modulus of the GO-*g*-PAN fibers were greatly enhanced as compared to the neat GO fibers, neat PAN fibers, and GO/PAN blending fibers. The covalent grafting of PAN on GO sheets has been demonstrated to the main attribution to the superior mechanical performance. The property might be further improved by further carbonization as used in the fabrication of PAN-based commercial carbon fibers. The realization of

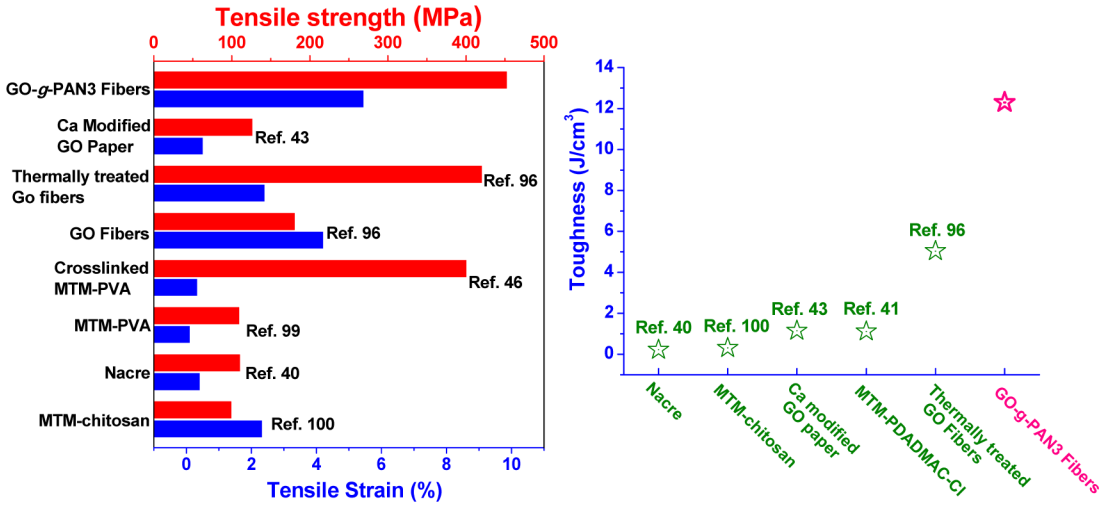

Figure 10. (a) Comparison of tensile strength and strain to a set of nanocomposites with layered structures. (b) Toughness comparison of GO-*g*-PAN3 fiber, nacre, and other biomimetic composites.

dx.doi.org/10.1021/ma400681v | *Macromolecules* 2013, 46, 6931–6941

continuous strong biomimetic fibers breaks new ground for the design and preparation of biomimics and high performance composites by introduction of covalent grafting to the inorganic and organic interfaces.

■ ASSOCIATED CONTENT

Supporting Information

GPC traces of free PAN isolated from polymerization samples, AFM images and the width distribution of GO-*g*-PAN3 sheets, fingerprint-like optical textures of GO-*g*-PAN CLCs, SAXS 2D patterns of GO-*g*-PAN CLCs depending on concentrations, SAXS data and Callié line shape analysis results of GO-*g*-PAN CLCs, list of mechanical performance for different biomimetic composites, and supplementary note. This material is available free of charge via the Internet at http://pubs.acs.org.

■ AUTHOR INFORMATION

Corresponding Author

*E-mail: chaogao@zju.edu.cn (C.G.).

Notes

The authors declare no competing financial interest.

■ ACKNOWLEDGMENTS

We acknowledge the kind suggestion of Professor Noel A. Clark at the University of Colorado on the calculation of Frank elastic constant. We thank the staffs of BL16B1 Beamline in the Shanghai Synchrotron Radiation Facility for SAXS characterizations and the supporting project (Z12sr0042). This work was supported by the National Natural Science Foundation of China (No. 51173162), Qianjiang Talent Foundation of Zhejiang Province (No. 2010R10021), Fundamental Research Funds for the Central Universities (No. 2013XZZX003), and Research Fund for the Doctoral Program of Higher Education of China (No. 20100101110049) and Zhejiang Provincial Natural Science Foundation of China (No. R4110175).

■ REFERENCES

(1) Novoselov, K. S.; Geim, A. K.; Morozov, S. V.; Jiang, D.; Zhang, Y.; Dubonos, S. V.; Grigorieva, I. V.; Firsov, A. A. *Science* **2004**, *306*, 666−669.
(2) Geim, A. K.; Novoselov, K. S. *Nat. Mater.* **2007**, *6*, 183−191.
(3) Geim, A. K. *Science* **2009**, *324*, 1530−1534.
(4) Novoselov, K. S.; Falko, V. I.; Colombo, L.; Gellert, P. R.; Schwab, M. G.; Kim, K. *Nature* **2012**, *490*, 192−200.
(5) Ruoff, R. *Nature* **2012**, *483*, S42−S42.
(6) Kim, K.; Choi, J. Y.; Kim, T.; Cho, S. H.; Chung, H. J. *Nature* **2011**, *479*, 338−344.
(7) Bekyarova, E.; Sarkar, S.; Wang, F.; Itkis, M. E.; Kalinina, I.; Tian, X.; Haddon, R. C. *Acc. Chem. Res.* **2012**, *46*, 65−76.
(8) Shao, Y.; Wang, J.; Wu, H.; Liu, J.; Aksay, I. A.; Lin, Y. *Electroanalysis* **2010**, *22*, 1027−1036.
(9) Brownson, D. A. C.; Kampouris, D. K.; Banks, C. E. *J. Power Sources* **2011**, *196*, 4873−4885.
(10) Huang, X.; Qi, X.; Boey, F.; Zhang, H. *Chem. Soc. Rev.* **2012**, *41*, 666−686.
(11) Krishnan, D.; Kim, F.; Luo, J.; Cruz-Silva, R.; Cote, L. J.; Jang, H. D.; Huang, J. *Nano Today* **2012**, *7*, 137−152.
(12) Yan, L.; Zheng, Y.; Zhao, F.; Li, S.; Gao, X.; Xu, B.; Weiss, P. S.; Zhao, Y. *Chem. Soc. Rev.* **2012**, *41*, 97−114.
(13) Zhu, Y.; James, D. K.; Tour, J. M. *Adv. Mater.* **2012**, *24*, 4924−4955.
(14) Chen, D.; Feng, H.; Li, J. *Chem. Rev.* **2012**, *112*, 6027−6053.
(15) Badri, A.; Whittaker, M. R.; Zetterlund, P. B. *J. Polym. Sci., Part A: Polym. Chem.* **2012**, *50*, 2981−2992.
(16) Dreyer, D. R.; Park, S.; Bielawski, C. W.; Ruoff, R. S. *Chem. Soc. Rev.* **2010**, *39*, 228−240.
(17) Compton, O. C.; Nguyen, S. T. *Small* **2010**, *6*, 711−723.
(18) Wan, X.; Huang, Y.; Chen, Y. *Acc. Chem. Res.* **2012**, *45*, 598−607.
(19) He, H.; Gao, C. *Molecules* **2010**, *15*, 4679−4694.
(20) Wu, D. Q.; Zhang, F.; Liang, H.; Feng, X. *Chem. Soc. Rev.* **2012**, *41*, 6160−6177.
(21) Kuilla, T.; Bhadra, S.; Yao, D.; Kim, N. H.; Bose, S.; Lee, J. H. *Prog. Polym. Sci.* **2010**, *35*, 1350−1375.
(22) Bai, H.; Li, C.; Shi, G. *Adv. Mater.* **2011**, *23*, 1089−1115.
(23) Liu, Z.; Zhang, X.; Yan, X.; Chen, Y.; Tian, J. *Chin. Sci. Bull.* **2012**, *57*, 2971−2982.
(24) Ren, L. L.; Liu, T. X.; Guo, J. A.; Guo, S. Z.; Wang, X. Y.; Wang, W. Z. *Nanotechnology* **2010**, *21*, 335701.
(25) Mineral Commodity Summaries: 2013; Olson, D. W., Ed.; Geological Survey, 2013; pp 68−69.
(26) A. G. Corp. Graphite uses and Future Demand; http://alabamagraphite.co/graphite-supply-demand/.
(27) Xu, Z.; Gao, C. *ACS Nano* **2011**, *5*, 2908−2915.
(28) Xu, Z.; Gao, C. *Nat. Commun.* **2011**, *2*, 571.
(29) Aboutalebi, S. H.; Gudarzi, M. M.; Zheng, Q. B.; Kim, J. K. *Adv. Funct. Mater.* **2011**, *21*, 2978−2988.
(30) Kim, J. E.; Han, T. H.; Lee, S. H.; Kim, J. Y.; Ahn, C. W.; Yun, J. M.; Kim, S. O. *Angew. Chem., Int. Ed.* **2011**, *50*, 3043−3047.
(31) Saha, A.; Palmal, S.; Jana, N. R. *Nanoscale* **2012**, *4*, 6649−6657.
(32) Senyuk, B.; Behabtu, N.; Pacheco, B. G.; Lee, T.; Ceriotti, G.; Tour, J. M.; Pasquali, M.; Smalyukh, I. I. *ACS Nano* **2012**, *6*, 8060−8066.
(33) Xu, Z.; Zhang, Y.; Li, P.; Gao, C. *ACS Nano* **2012**, *6*, 7103−7113.
(34) Xu, Z.; Sun, H.; Zhao, X.; Gao, C. *Adv. Mater.* **2012**, *25*, 188−193.
(35) Xu, Z.; Liu, Z.; Sun, H.; Zhao, X.; Gao, C. *Adv. Mater.* **2013**, *25*, 3249−3253.
(36) Hu, X.; Xu, Z.; Gao, C. *Sci. Rep.* **2012**, *2*, 767.
(37) Kou, L.; Gao, C. *Nanoscale* **2013**, *5*, 4370−4378.
(38) Jalili, R.; Aboutalebi, S. H.; Esrafilzadeh, D.; Shepherd, R. L.; Chen, J.; Aminorroaya-Yamini, S.; Konstantinov, K.; Minett, A. I.; Razal, J. M.; Wallace, G. G. *Adv. Funct. Mater.* **2013**, DOI: 10.1002/adfm.201300765.
(39) Chen, L.; He, Y.; Chai, S.; Qiang, H.; Chen, F.; Fu, Q. *Nanoscale* **2013**, *5*, 5809−5815.
(40) Yao, H.; Fang, H.; Wang, X.; Yu, S. *Chem. Soc. Rev.* **2011**, *40*, 3764−3785.
(41) Walther, A.; Bjurhager, I.; Malho, J.-M.; Ruokolainen, J.; Berglund, L.; Ikkala, O. *Angew. Chem., Int. Ed.* **2010**, *49*, 6448−6453.
(42) Ranjbartoreh, A. R.; Wang, B.; Shen, X.; Wang, G. *J. Appl. Phys.* **2011**, 109.
(43) Park, S.; Lee, K.-S.; Bozoklu, G.; Cai, W.; Nguyen, S. T.; Ruoff, R. S. *ACS Nano* **2008**, *2*, 572−578.
(44) Yao, H.; Tan, Z.; Fang, H.; Yu, S. *Angew. Chem., Int. Ed.* **2010**, *49*, 10127−10131.
(45) Bonderer, L. J.; Studart, A. R.; Gauckler, L. J. *Science* **2008**, *319*, 1069−1073.
(46) Podsiadlo, P.; Kaushik, A. K.; Arruda, E. M.; Waas, A. M.; Shim, B. S.; Xu, J.; Nandivada, H.; Pumplin, B. G.; Lahann, J.; Ramamoorthy, A.; Kotov, N. A. *Science* **2007**, *318*, 80−83.
(47) Lee, C.; Wei, X.; Kysar, J. W.; Hone, J. *Science* **2008**, *321*, 385−388.
(48) Suk, J. W.; Piner, R. D.; An, J.; Ruoff, R. S. *ACS Nano* **2010**, *4*, 6557−6564.
(49) Wang, X.; Bai, H.; Yao, Z.; Liu, A.; Shi, G. *J. Mater. Chem.* **2010**, *20*, 9032−9036.
(50) He, H.; Gao, C. *ACS Appl. Mater. Interfaces* **2010**, *2*, 3201−3210.
(51) Kou, L.; He, H.; Gao, C. *Nano-Micro Lett.* **2010**, *2*, 177−183.
(52) Xu, Z.; Gao, C. *Macromolecules* **2010**, *43*, 6716−6723.
(53) Kan, L.; Xu, Z.; Gao, C. *Macromolecules* **2011**, *44*, 444−452.

(54) Kan, L.; Zheng, B.; Gao, C. *Chin. Sci. Bull.* **2012**, *57*, 3026−3029.
(55) Yin, L.; Wang, J.; Lin, F.; Yang, J.; Nuli, Y. *Energy Environ. Sci.* **2012**, *5*, 6966−6972.
(56) Wu, F.; Lu, Y.; Shao, G.; Zeng, F.; Wu, Q. *Polym. Int.* **2012**, *61*, 1394−1399.
(57) Singh, V.; Tiwari, A.; Tripathi, D. N.; Sanghi, R. *J. Appl. Polym. Sci.* **2004**, *92*, 1569−1575.
(58) Korobeinyk, A. V.; Whitby, R. L. D.; Mikhalovsky, S. V. *Eur. Polym. J.* **2012**, *48*, 97−104.
(59) Veca, L. M.; Lu, F.; Meziani, M. J.; Cao, L.; Zhang, P.; Qi, G.; Qu, L.; Shrestha, M.; Sun, Y. P. *Chem. Commun.* **2009**, *18*, 2565−2567.
(60) Pasricha, R.; Gupta, S.; Srivastava, A. K. *Small* **2009**, *5*, 2253−2259.
(61) Lee, S.; Kim, Y.-J.; Kim, D.-H.; Ku, B.-C.; Joh, H.-I. *J. Phys. Chem. Solids* **2012**, *6*, 741−743.
(62) Ma, L.; Yang, X.; Gao, L.; Lu, M.; Guo, C.; Li, Y.; Tu, Y.; Zhu, X. *Carbon* **2013**, *53*, 269−276.
(63) Michot, L. J.; Bihannic, I.; Maddi, S.; Funari, S. S.; Baravian, C.; Levitz, P.; Davidson, P. *Proc. Natl. Acad. Sci. U. S. A.* **2006**, *103*, 16101−16104.
(64) Paineau, E.; Antonova, K.; Baravian, C.; Bihannic, I.; Davidson, P.; Dozov, I.; Impéror-Clerc, M.; Levitz, P.; Madsen, A.; Meneau, F.; Michot, L. J. *J. Phys. Chem. B* **2009**, *113*, 15858−15869.
(65) Kleshchanok, D.; Holmqvist, P.; Meijer, J. M.; Lekkerkerker, H. N. W. *J. Am. Chem. Soc.* **2012**, *134*, 5985−5990.
(66) Link, D. R.; Natale, G.; Shao, R.; Maclennan, J. E.; Clark, N. A.; Körblova, E.; Walba, D. M. *Science* **1997**, *278*, 1924−1927.
(67) Shirota, K.; Yaginuma, M.; Sakai, T.; Ishikawa, K.; Takezoe, H.; Fukuda, A. *Jpn. J. Appl. Phys., Part 1* **1996**, *35*, 2275−2279.
(68) Chandrasekhar, S.; Demus, D.; Goodby, J.; Gray, G.; Spiess, H. W.; Vill, V. *Handb. Liq. Cryst. Set* **2008**, 749−780.
(69) Lagerwall, J. P. F.; Scalia, G. *Curr. Appl. Phys.* **2012**, *12*, 1387−1412.
(70) Ihn, K. J.; Zasadzinski, J. A. N.; Pindak, R.; Slaney, A. J.; Goodby, J. *Science* **1992**, *258*, 275−278.
(71) Lei, N.; Safinya, C. R.; Bruinsma, R. F. *J. Phys. II* **1995**, *5*, 1155−1163.
(72) Ishikawa, T.; Lavrentovich, O. D. Defects and Undulation in Layered Liquid Crystals. In *Defects in Liquid Crystals: Computer Simulations, Theory and Experiments*; Lavrentovich, O., Pasini, P., Zannoni, C., Žumer, S., Eds.; Springer: Dordrecht, Netherlands, 2001; Vol. *43*, pp 271−300.
(73) de Gennes, P. G. *The Physics of Liquid Crystals*; Oxford University Press: New York, 1974.
(74) Gómez-Navarro, C.; Burghard, M.; Kern, K. *Nano Lett.* **2008**, *8*, 2045−2049.
(75) Holyst, R. *Phys. Rev. A* **1991**, *44*, 3692−3709.
(76) Sens, P.; Turner, M. S.; Pincus, P. *Phys. Rev. E* **1997**, *55*, 4394−4405.
(77) Das, M. M.; Das, B. M.; Saikia, M. D. *Structural Analysis*; PHI Learning Pvt. Ltd.: New Delhi, 2011.
(78) Dan, B.; Behabtu, N.; Martinez, A.; Evans, J. S.; Kosynkin, D. V.; Tour, J. M.; Pasquali, M.; Smalyukh, I. I. *Soft Matter* **2011**, *7*, 11154−11159.
(79) Laschat, S.; Baro, A.; Steinke, N.; Giesselmann, F.; Hägele, C.; Scalia, G.; Judele, R.; Kapatsina, E.; Sauer, S.; Schreivogel, A.; Tosoni, M. *Angew. Chem., Int. Ed.* **2007**, *46*, 4832−4887.
(80) Brown, W.; Mortensen, K. *Macromolecules* **1988**, *21*, 420−425.
(81) Gabriel, J.-C. P.; Camerel, F.; Lemaire, B. J.; Desvaux, H.; Davidson, P.; Batail, P. *Nature* **2001**, *413*, 504−508.
(82) Sun, D.; Sue, H.-J.; Cheng, Z.; Martínez-Ratón, Y.; Velasco, E. *Phys. Rev. E* **2009**, *80*, 041704.
(83) Miyazaki, S.; Karino, T.; Endo, H.; Haraguchi, K.; Shibayama, M. *Macromolecules* **2006**, *39*, 8112−8120.
(84) Carretero-González, J.; Castillo-Martínez, E.; Dias-Lima, M.; Acik, M.; Rogers, D. M.; Sovich, J.; Haines, C. S.; Lepró, X.; Kozlov, M.; Zhakidov, A.; Chabal, Y.; Baughman, R. H. *Adv. Mater.* **2012**, *24*, 5695−5701.
(85) Cong, H.; Ren, X.; Wang, P.; Yu, S. *Sci. Rep.* **2012**, *2*, 613.
(86) Chae, H. G.; Kumar, S. *Science* **2008**, *319*, 908−909.
(87) Huang, Y.; Liang, J.; Chen, Y. *Small* **2012**, *8*, 1805−1834.
(88) Zhang, P.; Jiang, K.; Ye, C.; Zhao, Y. *Chem. Commun.* **2011**, *47*, 9504−9506.
(89) He, H.; Gao, C. *Chem. Mater.* **2010**, *22*, 5054−5064.
(90) Young, R. J.; Kinloch, I. A.; Gong, L.; Novoselov, K. S. *Compos. Sci. Technol.* **2012**, *72*, 1459−1476.
(91) Wei, W. L.; Qu, X. G. *Small* **2012**, *8*, 2138−2151.
(92) Shen, J. F.; Yan, B.; Li, T.; Long, Y.; Li, N.; Ye, M. X. *Composites, Part A* **2012**, *43*, 1476−1481.
(93) Zhang, N. N.; Li, R. Q.; Zhang, L.; Chen, H. B.; Wang, W. C.; Liu, Y.; Wu, T.; Wang, X. D.; Wang, W.; Li, Y.; Zhao, Y.; Gao, J. P. *Soft Matter* **2011**, *7*, 7231−7239.
(94) Young, R. J.; Kinloch, I. A.; Nicolais, L. Graphene Composites. In *Wiley Encyclopedia of Composites*; John Wiley & Sons, Inc.: New York, 2011.
(95) Kim, H.; Abdala, A. A.; Macosko, C. W. *Macromolecules* **2010**, *43*, 6515−6530.
(96) Dong, Z.; Jiang, C.; Cheng, H.; Zhao, Y.; Shi, G.; Jiang, L.; Qu, L. *Adv. Mater.* **2012**, *24*, 1856−1861.
(97) Zhong, D.; Yang, Q.; Guo, L.; Liu, K.; Jiang, L. *Nanoscale* **2013**, *5*, 5758−5764.
(98) Jackson, A. P.; Vincent, J. F. V.; Briggs, D.; Crick, R. A.; Davies, S. F.; Hearn, M. J.; Turner, R. M. *J. Mater. Sci. Lett.* **1986**, *5*, 975−978.
(99) Tang, Z.; Kotov, N. A.; Magonov, S.; Ozturk, B. *Nat. Mater.* **2003**, *2*, 413−418.
(100) Jackson, A. P.; Vincent, J. F. V.; Turner, R. M. *Proc. R. Soc. London, B* **1988**, *234*, 415−440.